

FULL ARTICLE

Artefact reduction for cell migration visualization using spectral domain optical coherence tomography

Bernd Hofer^{1,2,3}, Boris Považay^{1,2}, Boris Hermann^{1,2}, Sara M. Rey², Vedran Kajić², Alexandre Tumlinson², Kate Powell², Gerald Matz³, and Wolfgang Drexler^{*,1,2}

¹ Center of Medical Physics and Biomedical Engineering, Medical University Vienna, Währinger Gürtel 18–20, 1090 Vienna, Austria

² Biomedical Imaging Group, School of Optometry and Vision Sciences, Cardiff University, Maindy Road, Cardiff, CF24 4LU, United Kingdom

³ Institute of Communications and Radio-Frequency Engineering, Vienna University of Technology, Gusshausstraße 25/389, 1040 Vienna, Austria

Received 10 October 2010, revised 17 December 2010, accepted 19 December 2010

Published online 13 January 2011

Key words: tomography, optical coherence, microscopy, cell physiological phenomena, image processing, computer-assisted, imaging, three-dimensional, biomedical engineering

Visualization of cell migration during chemotaxis using spectral domain optical coherence tomography (OCT) requires non-standard processing techniques. Stripe artefacts and camera noise floor present in OCT data prevent detailed computer-assisted reconstruction and quantification of cell locomotion. Furthermore, imaging artefacts lead to unreliable results in automated texture based cell analysis.

Here we characterize three pronounced artefacts that become visible when imaging sample structures with high dynamic range, e.g. cultured cells: (i) time-varying fixed-pattern noise; (ii) stripe artefacts generated by background estimation using tomogram averaging; (iii) image modulations due to spectral shaping. We evaluate techniques to minimize the above mentioned artefacts using an 800 nm optical coherence microscope. Effect of artefact reduction is shown exemplarily on two cell cultures, i.e.

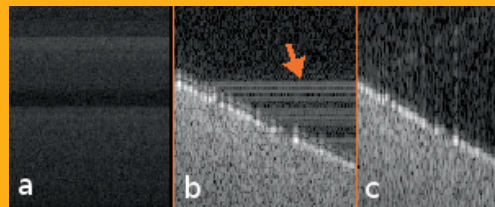


Figure showing artefacts present in OCT images. (a) camera noise floor; (b) stripe artefacts; (c) image modulations. These artefacts lead to inaccurate results in automated computer assisted image analysis.

Dictyostelium on nitrocellulose substrate, and retinal ganglion cells (RGC-5) cultured on a glass coverslip. Retinal imaging also profits from the proposed processing techniques.

1. Introduction

Biology-motivated biosciences necessitate cell imaging in 3D and 4D (3D cell observation over time). Substrates involved are often opaque which causes difficulties for conventional cellular imaging modalities such as differential interference contrast (DIC) microscopy. Therefore optical coherence tomogra-

phy (OCT) has been proposed to be used for time lapse cell imaging in 3D scaffolds [1–5]. Difficulties arise since OCT signals from cell samples exhibit high dynamic range. This can cause problems when using standard signal processing routines for image formation.

Recent advances in resolution and speed have enabled use of OCT for cell imaging. Small volumes

* Corresponding author: e-mail: wolfgang.drexler@meduniwien.ac.at

have been demonstrated with time domain (TD) systems at resolutions of $< 1 \mu\text{m}$ [6, 7]. Optical coherence microscopy (OCM) using *en face* TD detection offers the benefit of coherence gating [1, 8]. Acquisition speed and sensitivity was increased by using spectral domain (SD) OCT [9] and with numerical techniques transversal resolution could be retained outside focus region [10, 11]. One of the limits of 3D deconvolution is that it tends to reduce the sensitivity by the introduction of noise [11] and because of the required high phase stability it could not be applied to *in vivo* imaging [10]. SD-OCT has been applied to cellular imaging [2–5] and also offers the benefit of increased phase stability [12–15].

Swept source (SS) OCT benefits from dual balanced detection and does not necessarily require signal processing for background elimination (auto-correlation of source spectrum and fixed-pattern noise). SD-OCT in the 800 nm region currently outperforms SS-OCT in terms of resolution due to the availability of broadband lasers. Also SD-OCT now achieves ultra high-speed, comparable to the fastest available SS-OCT systems due to advances in camera technology [16–18]. However, SD-OCT requires a significant amount of signal processing for background handling and resampling.

Background handling for SD-OCT was previously proposed and successfully applied for retinal imaging. An independent measurement by blocking light in the sample arm was proposed [9] but does not account for source fluctuations during acquisition of 3D datasets or complicates measurement procedure when a shutter needs to be included. In fact, we investigated measuring the background light intensity independently, but found it not reliable. The results were strongly depending on the current light source stability. In time-lapse measurements over longer time periods (2 hours), a 3D volume was measured every 2 minutes [5]. Manually blocking in order to measure the background is impractical in this case. For this reason, we used the following approach: The background signal is estimated directly from the tomogram data [19]. By using the mean of the spectral B-scan data as estimate for source spectrum and fixed-pattern noise, background elimination by subtraction can be effectively achieved. This procedure assumes that heterogeneous sample structures will average out due to random phase contributions.

We have found that for OCT signals with high dynamic range the averaged background signal features a significant bias which can cause distortions in tomograms [20]. We verified experimentally that the reason for this bias is a skewed probability distribution of the detected signal, i.e. the phase distribution in the A-lines is not random. The averaged spectrum still contains structural information, originating from the strong scatterers. This is the motivation for proposing a novel background elimination

procedure that uses median-based background signal estimation that better accounts for the sample statistics. We also show that retinal imaging can benefit from this scheme.

Furthermore we demonstrate reduction of camera noise floor by spread-domain filtering. In tomograms this noise might be negligible and not very obvious because of masking by sample structure. However, the proposed techniques are necessitated to achieve more robust automated image evaluation. Quantification of cell locomotion and pattern analysis partially failed otherwise. Results were strongly dependent on the actual position of the individual cells. In addition we adapt spectral shaping in order to prevent modulation artefacts.

2. Theoretical background

With spectral domain OCT the signal $S(\omega, x)$ detected by the spectrometer depending on optical frequency ω and transversal position x can be expressed as [9, 21]

$$S(\omega, x) = \tilde{S}(\omega, x) + \bar{S}(\omega, x) + N(\omega, x) + W(\omega) + \tilde{W}(\omega, x) \quad (1)$$

where $\tilde{S}(\omega, x)$ is the interference spectrum required for tomogram generation, $\bar{S}(\omega, x)$ represents interferometric autocorrelation terms, $N(\omega, x)$ is stochastic measurement noise (e.g. thermal and shot noise), $W(\omega)$ is fixed-pattern noise of the camera, and $\tilde{W}(\omega, x)$ is time-varying¹ fixed-pattern (TVFP) noise. $W(\omega)$ and $\tilde{W}(\omega, x)$ can easily be suppressed by filtering since both terms are deterministic. The constant term $W(\omega)$ can be predetermined and subtracted from $S(\omega, x)$; alternatively, it can be included when estimating and subtracting the autocorrelation signal $\bar{S}(\omega, x)$. The camera specific time-varying term $\tilde{W}(\omega, x)$ can be suppressed by applying a time/spread-frequency filter (spread domain filter) that can be predetermined for each individual choice of transversal scan number N_x and acquisition speed.

Considering a simple model with a sample comprised of several reflective sites (with index k , not to be confused with the wavenumber); with $I_s^{(k)}(\omega, x)$ and $\tau_k(x)$ respectively denoting the frequency-dependent intensities and position-dependent optical delays, the interference signal in (1) can be written as

$$\tilde{S}(\omega, x) = 2 \Re \left\{ \sum_k \sqrt{I_r(\omega, x) I_s^{(k)}(\omega, x)} e^{j(\omega \tau_k(x) + \varphi(\omega))} \right\} \quad (2)$$

¹ More precisely, position-varying.

Here, $\varphi(\omega)$ is the dispersive phase and $I_r(\omega, x) = |E_r(\omega, x)|^2$ is the reference arm intensity that depends on acquisition time (related to x via camera line rate). For the autocorrelation terms we likewise obtain

$$\begin{aligned} \bar{S}(\omega, x) &= |E_r(\omega, x)|^2 + |E_s(\omega, x)|^2 = I_r(\omega, x) \\ &+ \sum_k \sum_m \sqrt{I_s^{(k)}(\omega, x) I_s^{(m)}(\omega, x)} e^{j(\omega(\tau_k(x) - \tau_m(x)))} \end{aligned} \quad (3)$$

When the sample arm intensities are small, $|E_s(\omega, x)|^2$ may be neglected and $\bar{S}(\omega, x)$ can be well approximated by the time-averaged electric field $|E_r(\omega, x)|^2$ returning from the reference arm, i.e., $\bar{S}(\omega, x) \approx I_r(\omega, x)$ does not depend on the specific sample structure. The time dependence of $\bar{S}(\omega, x)$ due to source fluctuations may also be neglected, when the acquisition time for a tomogram is short (e.g. the experimental setup described below requires 26 ms to capture $N_x = 512$ depth scans). Although it is possible to directly measure $I_r(\omega)$ and $W(\omega)$ by blocking the sample arm before B-scan acquisition, a typical approach based on the above assumptions is to simply average the data from all depth scans within a tomogram, i.e., $\bar{S}(\omega) + W(\omega) \approx \langle S(\omega, x) \rangle_x$ given that $\langle S(\omega, x) \rangle_x \approx 0$. However, practical samples do not have a fully homogeneous structure and $\bar{S}(\omega, x)$ will not be zero mean, resulting in background artefacts that become visible in the final tomograms.

3. Methods

A fibre based spectral domain OCT system adapted for high bandwidth throughput of 130 nm at 800 nm was used for acquisition of experimental data [5]. A scanning microscope was employed as sample probe with the objective having 10 mm working distance, a numerical aperture of ~ 0.1 and power on sample with 2 mW. Sensitivity close to zero delay position was 94 dB, signal loss at 1000 μm was about -8 dB, and resolution quantified as $2.9 \pm 0.05 \mu\text{m}$ in air. Signal loss at maximum depth range of 1370 μm was 17 dB.

A block diagram of the various signal processing tasks involved in spectral domain OCT tomogram generation is shown in Figure 1. Please note, that we are interested in suppression of two components:

1. time varying camera noise, i.e. TVFP,
2. and artefacts due to wrong background estimation.

TVFP reduction needs to be processed *before* resampling, because otherwise the TFVP noise would spread out in spatial domain after Fourier transform. On the other hand, background estimation and correction has to be computed *after* resampling, because the artefacts originate from actual sample structure.

Current implementations typically have fixed-pattern noise reduction and background correction combined to a single processing step (cf. [19, 22]) which is followed by spectral resampling. With the proposed procedure, suppression of TVFP noise (i.e. the camera specific variation of noise between sequential A-lines) becomes an independent first processing step.

Background correction and resampling are shown as a combined processing task. Contrary to current approaches, where resampling happens after background subtraction, our novel median-based background estimation operates on the resampled data to achieve best results.

The resulting interference spectrum is passed to the final correction block. Here, spectral shaping adjusts the envelope of the interference spectrum to minimize sidelobes of signal peaks; furthermore, dispersion compensation changes the phase of the interference spectrum to maximize tomogram resolution. The corrected interference spectrum is transformed to the spatial domain via inverse FFT and the final tomograms are obtained by viewing signal magnitude on a logarithmic scale.

TVFP noise reduction The proposed TVFP noise reduction scheme is depicted in Figure 2. The schematic in Figure 2(a) shows connections of different representations of the data via Fourier transform. With blocked light source, the output signal of the spectrometer only contains fixed-pattern noise terms when neglecting stochastic noise $N(\omega, x)$, i.e., $S(\omega, x) = W(\omega) + \tilde{W}(\omega, x)$. The tomograms shown in Figure 2 have $N_t = 1024$ depth pixels, $N_x = 512$ A-lines, and amplitudes shown in dB using a gray scale representing a dynamic range of 35 dB.

Conventional processing determines the fixed-pattern noise by averaging all depth scans, i.e., $W(\omega) = \langle S(\omega, x) \rangle_x$ ($\tilde{S}(\omega, x) = 0$; $\bar{S}(\omega, x) = 0$, because the light source is blocked), and computing the TVFP noise from the raw data as $\tilde{W}(\omega, x) = S(\omega, x) - \langle S(\omega, x) \rangle_x$. After spectral resampling of the data

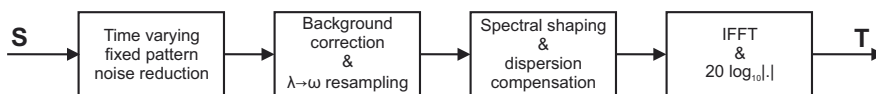


Figure 1 Block diagram of the proposed artefact reduction scheme for constructing tomograms $T(\tau, x)$ from spectral domain raw data $S(\omega, x)$.

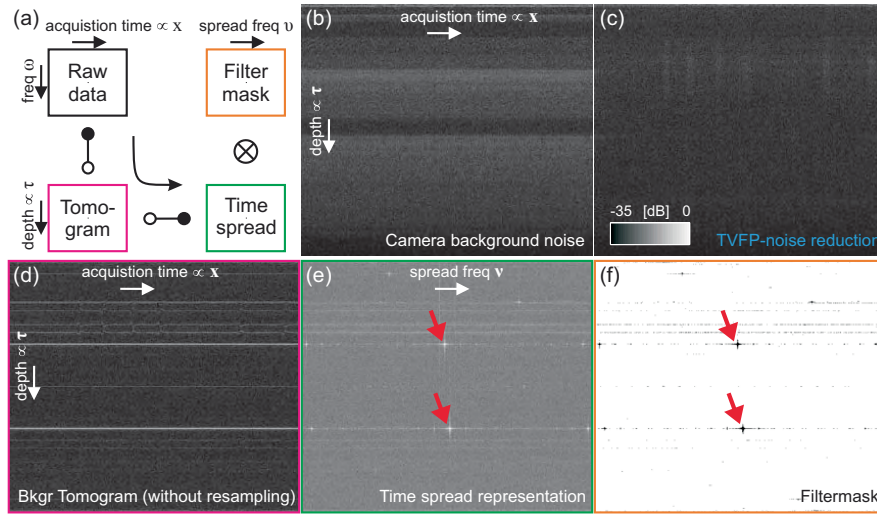


Figure 2 (a) TVFP noise suppression scheme, (b) tomogram of camera background noise after mean background subtraction and resampling, (c) tomogram with additional TVFP noise reduction, (d) tomogram of TVFP noise before resampling, (e) spread domain representation of TVFP noise, red arrows indicate dominating high intensity locations, (f) binary filter mask for TVFP-noise reduction (black = 0, white = 1).

from pixel-dependent optical frequency $\omega = \omega_p$ to uniformly spaced frequencies ω_u [21], the TVFP tomogram $T_{\text{TVFP}}(\tau, x) = \mathcal{F}_{\omega \rightarrow \tau}^{-1} \{ \tilde{W}(\omega, x) \}$ is obtained via a Fourier transformation (see Figure 2(b)). Since the camera background noise is not spatially uniform, disturbing horizontal bands with larger average intensity become visible. Often, camera-specific TVFP will be covered by shot noise of typical tomograms (see the discussion below).

Figure 2(d) shows the TVFP tomogram $\tilde{T}_{\text{TVFP}}(\tau, x)$ obtained by omitting the spectral resampling. Here, TVFP noise is spatially concentrated on a few horizontal lines, demonstrating that the depth-broadening of TVFP noise in Figure 2(b) is caused by the resampling. Figure 2(e) shows the depth-spread representation² $V_{\text{TVFP}}(\tau, \nu) = \mathcal{F}_{x \rightarrow \nu} \{ \tilde{T}_{\text{TVFP}}(\tau, x) \}$ that is obtained by applying a transversal Fourier transform to the TVFP tomogram $\tilde{T}_{\text{TVFP}}(\tau, x)$. Here, the horizontal TVFP noise tomogram lines manifest themselves as strong peaks (indicated by red arrows). To reduce TVFP noise, we designed a binary filter mask (cf. Figure 2(f)) as

$$U(\tau, \nu) = \begin{cases} 0 & |V_{\text{TVFP}}(\tau, \nu)| > \gamma V_{0.5} \\ 1 & \text{else} \end{cases} \quad (4)$$

where $V_{0.5}$ denotes the median of $|V_{\text{TVFP}}(\tau, \nu)|$ and the thresholding factor was empirically chosen as $\gamma = 5$ (with this choice, 0.4% of the depth-spread-domain pixels are suppressed). The depth-spread domain filter for TVFP reduction may be described as binary notch filter and involves the following steps:

- transformation of the raw data to the depth-spread domain:

$$V(\tau, \nu) = \mathcal{F}_{x \rightarrow \nu} \{ \mathcal{F}_{\omega \rightarrow \tau}^{-1} \{ S(\omega, x) \} \} \quad (5)$$

- TVFP noise suppression using the filter mask:

$$\tilde{V}(\tau, \nu) = V(\tau, \nu) U(\tau, \nu) \quad (6)$$

- transformation of the filter output to the spectral domain:

$$\hat{S}(\omega, x) = \mathcal{F}_{\tau \rightarrow \omega} \{ \mathcal{F}_{\nu \rightarrow x}^{-1} \{ \tilde{V}(\tau, \nu) \} \} \approx S(\omega, x) - \tilde{W}(\omega, x) \quad (7)$$

All operations in (4)–(7) are performed before resampling, resulting in minimal distortion of tomogram data through the sparse filter mask. The resulting tomogram after resampling and subtraction of $W(\omega)$ is shown in Figure 2(c). Compared with Figure 2(b) the noise floor is substantially reduced.

Background elimination As described in Section 2, with standard processing the background signal $\tilde{S}(\omega) + W(\omega)$ is estimated by transversally averaging the raw data [19], i.e.,

$$B_{\text{mean}}(\omega) = \langle S(\omega, x) \rangle_x \quad (8)$$

and afterwards subtracted (cf. Figure 3(a)) according to

$$\tilde{\tilde{S}}(\omega, x) = S(\omega, x) - B_{\text{mean}}(\omega) f(x) \quad (9)$$

where the coefficients

$$f(x) = \frac{\langle B_{\text{mean}}(\omega) S(\omega, x) \rangle_\omega}{\langle B_{\text{mean}}^2(\omega) \rangle_\omega} \quad (10)$$

account for energy fluctuations of the background signal between successive tomogram lines. These fluctuations are caused by timing issues within the CCD-electronics of the camera and by laser instabilities [21]. Background subtraction is then followed by spectral resampling from $\omega = \omega_p$ to ω_u .

The block diagram of the proposed background elimination scheme is depicted in Figure 3(b).

² Here, ν denotes spread frequency [23].

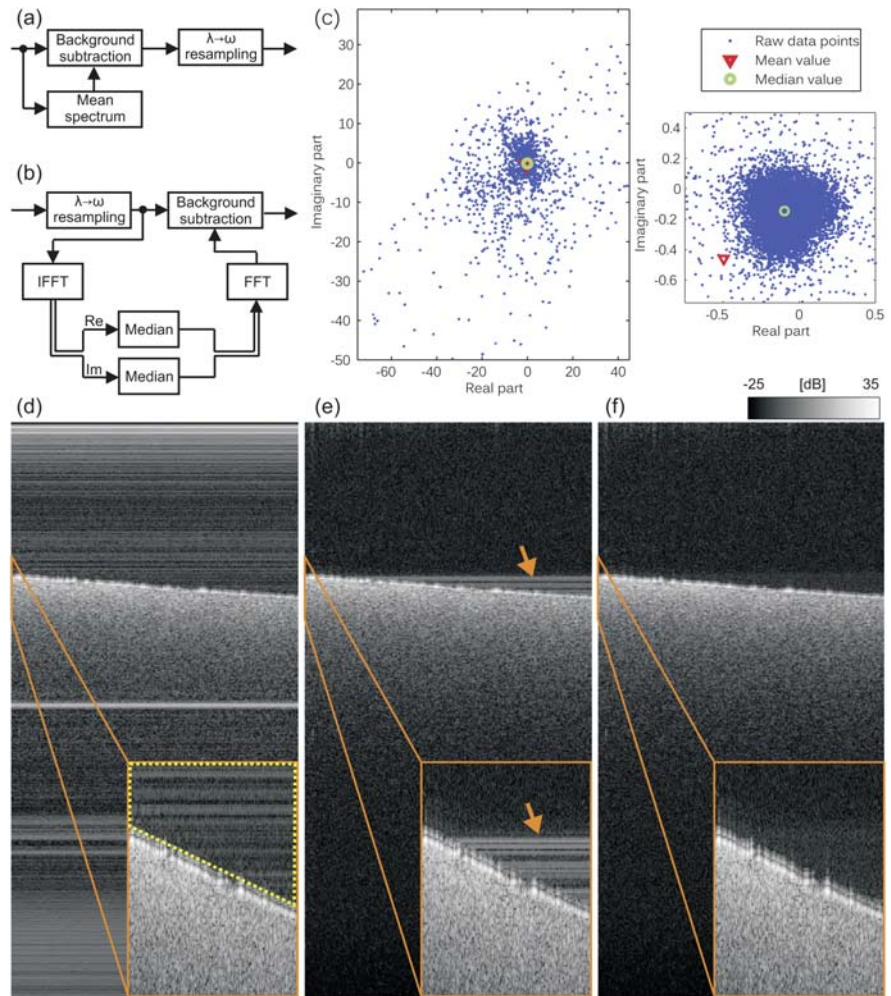


Figure 3 Proposed background elimination procedure; (a) block diagram of standard approach, (b) block diagram of proposed scheme, (c) amplitude distribution of complex tomogram data corresponding to a depth indicated by orange arrow, (d) tomogram of black nitrocellulose filter without background elimination, (e) tomogram after mean background subtraction, (f) median-based background subtraction. Vertically zoomed tomogram portions are shown within the orange frames.

Contrary to the previously described background subtraction, here, the raw data is first resampled which amounts to obtaining a sharp time-domain representation of the sample structures in the tomogram $T(\tau, x) = \mathcal{F}_{\omega \rightarrow \tau}^{-1}\{S(\omega_u, x)\}$. A complex-valued background signal is then estimated in the time domain using transversal median values and transformed back to the frequency domain:

$$B_{\text{median}}(\omega) = \mathcal{F}_{\tau \rightarrow \omega}\{\text{median}_x\{\Re\{T(\tau, x)\}\} + j \text{median}_x\{\Im\{T(\tau, x)\}\}\} \quad (11)$$

The background signal is then subtracted in the frequency domain according to (9), (10) with $B_{\text{mean}}(\omega)$ replaced with $B_{\text{median}}(\omega)$ (subtraction directly on complex tomogram data is equivalently possible). While the averaging in (8) can equivalently be performed in the time-domain, computing the (complex) median in the spectral domain is not equivalent to (11) since the median is a non-linear operation that does not commute with the Fourier transform.

To illustrate the procedure and describe the difference to standard background estimation, a black nitrocellulose filter was measured. The tomogram of resampled raw data consisting of 1024 depth pixels and 512 transversal pixels is shown in Figure 3(d); horizontal lines are due to the background signal. The slightly tilted surface of the filter is highly scattering. Mean background subtraction introduces horizontal line artefacts above the filter surface and strongly disturbs parts of the tomogram, cf. Figure 3(e). Figure 3(c) shows a scatter-plot of the complex tomogram data at the depth indicated by the orange arrow in Figure 3(e). The high intensity signal parts corresponding to the filter surface cause the distribution of the real and imaginary part of $T_{(\tau_k, x)}$ to be strongly skewed, resulting in a significant bias when estimating the background signal via (8). Viewing the desired strong signal components as outliers with regard to the background distribution suggests the use of more robust nonlinear estimators. Specifically, median based background estimation according to (11) after resampling of the data is

insensitive to strong signal components and provides a robust estimate of the background signal. This is illustrated in the zoomed portion in Figure 3(c): the median (green circle) better represents the centroid of the actual background whereas the mean (red triangle) features a significant bias. Using the median-based background estimate (11) for background subtraction results in an improved tomogram that is free of horizontal line artefacts, see Figure 3(f). We verified for different samples that simply replacing mean by median in (8) results in poorer background artefact suppression than with the proposed procedure. This can be attributed to the fact that high-intensity peaks are better localized *after* resampling and can then be better suppressed by the median-based background estimator. We note that TVFP noise suppression was not used for the tomograms in Figure 3. TVFP noise is visible in the slightly increased noise floor above the filter surface in Figure 3(f); this will be further verified in Figure 4.

Spectral shaping A Gaussian-shaped source spectrum is advantageous in OCT since it results in a narrow axial point-spread function (PSF) with mini-

mal side-lobes. However, the spectrum of available light sources often deviates from Gaussian or other suitable smooth spectral shapes. Source spectral shaping is possible but complicates the optical setup [24, 25]. Therefore, several numerical apodization techniques have been proposed for PSF optimization on data from time-domain OCT [26–30] and frequency-domain OCT [31, 32]. All techniques involve deconvolution with an estimated or measured spectral envelope. Whereas in early approaches the spectrum was determined from measurements of a single reflecting surface [26–28], more recent approaches demonstrate that source fluctuations can be handled with estimation from tomogram data [29, 31, 32]. When reduction of axial measurement range can be accepted, apodization on individual depth scans can be performed even for very unstable light sources; here, spatial domain filtering allows extraction of the source spectrum as demonstrated in [31].

We adapt the shaping procedure proposed for FD-OCT data in [32] which is also suitable for full range imaging and accounts for polarization mismatch and source fluctuations on individual tomograms. According to [32], the interference signal

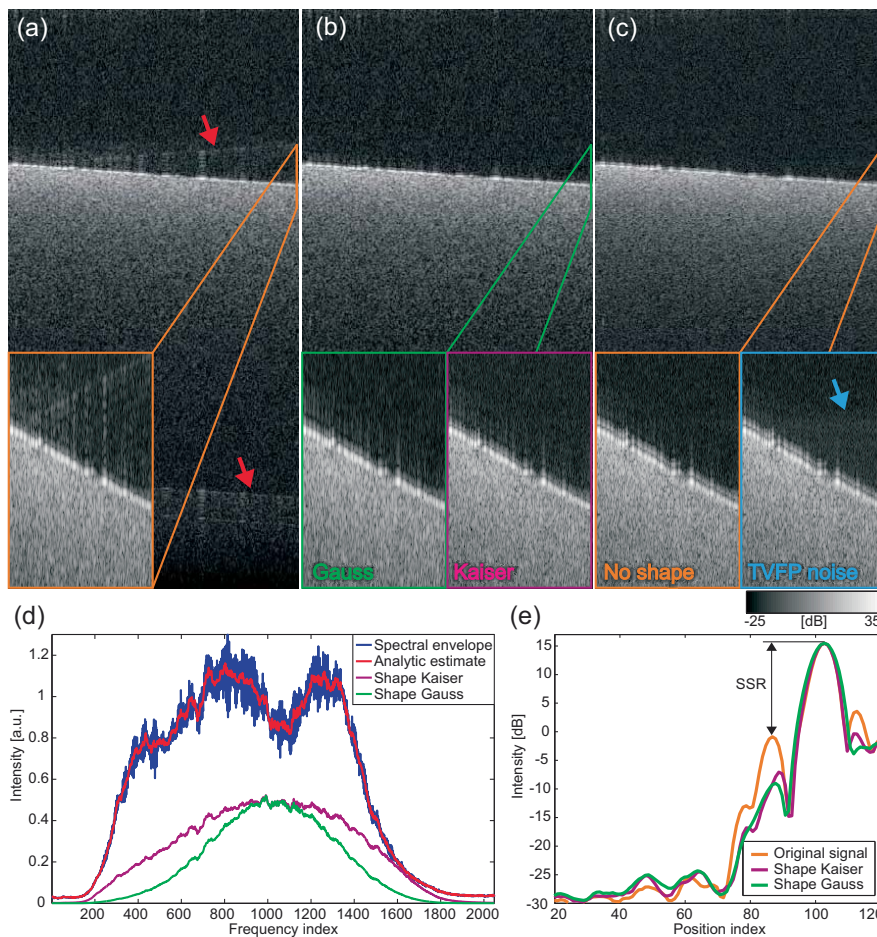


Figure 4 Spectral shaping without modulation artefact. (a) Gaussian shape with conventional estimate of spectral envelope, modulation artefacts indicated by red arrows; (b) shaping with Gaussian and Kaiser window; (c) No shaping, blue arrow indicates TVFP noise; (d) resulting estimates of spectral envelopes and shape functions; (e) achieved sidelobe suppression ratio (SSR) at nitrocellulose filter surface.

$\tilde{S}(\omega, x)$ in (2) can be rewritten using the spectral envelope $\check{S}(\omega)$, the local scattering amplitude $a_k(x)$ and phase $\varphi_k(\omega, x) = \omega\tau_k(x) + \varphi(\omega)$ as

$$\tilde{S}(\omega, x) = \check{S}(\omega) 2 \sum_k a_k(x) \cos(\varphi_k(\omega, x)) \quad (12)$$

Assuming that $\varphi_k(\omega, x)$ is uniformly distributed within $[-\pi, \pi]$, that $a_k(x)$ is Rayleigh distributed with variance $a/2$, and that $a_k(x)$ and $\varphi_k(\omega, x)$ are statistical independent, $\check{S}(\omega)$ can be estimated from tomogram data as

$$\check{S}(\omega) = \sqrt{\frac{1}{2a} \langle |\tilde{S}(\omega, x)|^2 \rangle_x} \quad (13)$$

since we have the ensemble averages $\langle |a_k(x)|^2 \rangle = a$ and $\langle |\cos(\varphi_k(\omega, x))|^2 \rangle = 1/2$. Spectral shaping using a Wiener filter approach amounts to

$$\tilde{S}_{\text{shape}}(\omega, x) = G(\omega) \frac{\check{S}(\omega)}{\check{S}(\omega)^2 + \eta} \tilde{S}(\omega, x) \quad (14)$$

with the apodization window $G(\omega)$ determining resolution and sidelobe suppression and the parameter η trading off bias versus noise amplification. Eq. (13) cannot be used if the tomogram data exhibits structural correlations e.g. those arising from reflective substrate surfaces such as the nitrocellulose filter shown in Figure 3. Thus, we propose to estimate the spectral envelope by replacing $\tilde{S}(\omega, x)$ in (13) with the analytic interference signal $\tilde{S}_A(\omega, x) = [\tilde{S}(\omega, x) + j \mathcal{H}\{\tilde{S}(\omega, x)\}]/\sqrt{2}$.

To explain the difference, we consider the spectral fringes from the nitrocellulose filter surface (cf. Figure 3(c)). From (12) the simplified interference signal of the plain surface can be expressed as $\tilde{S}(\omega, x) = a(x) \check{S}(\omega) 2 \cos(\omega(\tau_0 + \Delta\tau x))$, where τ_0 corresponds to the surface position on the left side of the tomogram, and surface tilt is determined by $\Delta\tau$. Here, we obtain

$$\langle |\tilde{S}(\omega, x)|^2 \rangle_x = 2a\check{S}^2(\omega) \underbrace{(1 + \langle \cos(2\omega(\tau_0 + \Delta\tau x)) \rangle_x)}_{\tilde{G}(\omega) \neq 0} \quad (15)$$

Thus, the average contains modulation frequencies $\tilde{G}(\omega)$ because of the deterministic surface tilt $\Delta\tau$. In contrast, despite the structural correlation the average power of the analytic interference signal $\tilde{S}_A(\omega, x) = \sqrt{2} a(x) \check{S}(\omega) \exp(j\omega(\tau_0 + \Delta\tau x))$ reads

$$\begin{aligned} \langle |\tilde{S}_A(\omega, x)|^2 \rangle_x &= 2a\check{S}^2(\omega) \langle e^{j\omega(\tau_0 + \Delta\tau x)} e^{-j\omega(\tau_0 + \Delta\tau x)} \rangle_x \\ &= 2a\check{S}^2(\omega) \end{aligned} \quad (16)$$

The improvement of the proposed envelope estimation procedure over conventional envelope estimation is illustrated in Figure 4. Using a Gaussian window and the conventional estimate, (13) results in reduced sidelobes (Figure 4(a)), however the modulation terms $\tilde{G}(\omega)$ impinging on the spectral envelope (blue curve in Figure 4(d)) cause stripe artefacts indicated by red arrows in Figure 4(a). With the ‘‘analytic’’ envelope estimation, modulation terms on the spectral envelope are substantially reduced (red curve in Figure 4(d)) and spectral shaping can be achieved without introducing artefacts as seen by comparing Figure 4(b) (tomograms with shaping) and Figure 4(c) (tomogram without shaping). Average signals from the strongly reflecting nitrocellulose filter surface are depicted in Figure 4(e), which demonstrates the achievable sidelobe suppression ratio (SSR) at the first (strongest) sidelobe of the surface achieved with $\eta = 0.01$ (obtained empirically for the current system). Without spectral shaping, an SSR of 15 dB is observed. A Kaiser shaping window improves the SSR by 6 dB without resolution loss. With a Gaussian window, the SSR is increased by 9 dB at the cost of a 0.5 μm resolution loss. The spectral envelopes shaped using the Wiener filter (14) with a Kaiser window (magenta curve) and Gaussian window (green curve) are shown in Figure 4(d). The tomograms have been obtained with TVFP noise reduction; without TVFP noise reduction, an increased noise floor above the filter surface (marked by blue arrow) remains (see the zoom in Figure 4(c)).

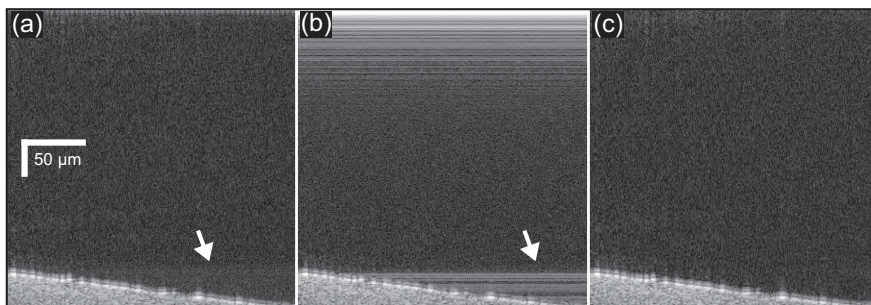
4. Results and discussion

Table 1 presents background suppression ratio (BSR), SSR and computational time for different processing methods on data from black nitrocellulose filter (1024 depth pixels, 512 A-lines). BSR is calculated as ratio of average surface signal to average background signal within a region of interest (ROI) above the first sidelobe (yellow dotted frame in Figure 3(d)). Processing without background correction serves as a baseline and includes resampling, FFT and dB conversion (cf. Table 1(a), Figure 3(d)). With background subtraction based on blocking the sample light [9] an increase of BSR by 4.7 dB is achieved (cf. Table 1(b), Figure 5(a)). The median based background reduction technique (c.f. Table 1(e)) resulted in the same BSR increase and a nearly identical tomogram (cf. Figure 3(f)) at the cost of a 35% increase in computation time.

Median based background estimation on individual tomograms is more robust than measuring the background before imaging of each 3D dataset since spectrum fluctuations of the employed light source (Integral, Femtolasers, Vienna, Austria) can occur within volume acquisition (cf. Figure 7(d)). Also the employed scanning microscope prevented implementation of a shutter which would have been necessary for rapid automated background measurement in time-lapse imaging [5]. Fixed pattern suppression ac-

Table 1 Evaluation of Background suppression ratio (BSR) and sidelobe suppression ratio (SSR) for different processing methods on tomogram from black nitrocellulose filter (cf. Figures 3–5). Calculation times for Matlab implementation with single core processing on Intel 2 GHz, 1.2 GB RAM.

processing method	BSR [dB]	SSR [dB]	comp. time [s]
(a) No correction	40.1	16.4	1.36
(b) Blocked sample [9]	44.8	16.4	1.37
(c) Fixed pattern suppression [22]	41.1	16.4	1.41
(d) Mean background subtraction [19]	41.4	16.4	1.41
(e) Median background subtraction (11)	44.8	16.5	1.83
(f) TVFP reduction followed by (e)	46.0	16.5	2.22
(g) (f) and background shaping with Gaussian	45.6	19.5	2.26
(h) (f) and background shaping with Kaiser	45.8	18.0	2.26
(i) (f) and spectral envelope shaping Gaussian	45.4	25.5	2.89
(j) (f) and spectral envelope shaping Kaiser	45.6	23.4	2.89

**Figure 5** Images used for evaluation of background suppression as summarized in Table 1. (a) background measured by blocking the sample arm, cf. Table 1(b) [9]. TVFP noise is not suppressed as indicated by white arrow. (b) fixed pattern suppression according to [22], cf. Table 1(c); (c) median background estimation and TVFP suppression, cf. Table 1(f). Images include first 310 depth pixels (415 μm in air) from zero delay position down to surface of nitrocellulose filter.

cording to [22] (cf. Table 1(c), Figure 5(b)) and mean background subtraction [19] achieve a BSR increase of about 1 dB but both methods exhibit similar horizontal line artifacts (cf. Figures 3(e) and 5(b) for mean background subtraction) and therefore cannot be used with our samples. The highest BSR increase by 5.9 dB is achieved with additional application of the TVFP reduction scheme (cf. Table 1(f), Figure 5(c)) at the cost of a 63% increase in computation time. If the background spectrum (11) is used for spectral shaping, the SSR is increased by 3 dB/1.5 dB with a Gaussian/Kaiser window. By employing the spectral envelope according to (13) a SSR increase of 9.1 dB/6 dB is achieved with a Gaussian/Kaiser window at the cost of a further 28% increase in computation time as compared to shaping with the background spectrum. Spectral shaping reduces the maximum achievable BSR increase by about 0.5 dB because higher order sidelobes are slightly amplified due to the reduced bandwidth of the shaping window.

The proposed processing steps as described in the previous section have been experimentally evaluated using *Dictyostelium discoideum* [5] on a white nitrocellulose filter in Figure 6 and RCG-5 cells [33]

on glass coverslips in Figure 7. Dynamic range in Figures 6 and 7 is 60 dB. Further results on visualization of cell migration achieved with the here presented artefact reduction techniques can be found in [5].

As described in [5] *Dictyostelium* is a social unicellular amoeba that forms multicellular structures of 10000 cells when starved of nutrients. Such a multicellular structure forming a mound on the filter surface is depicted in Figure 6. Here TVFP noise was masked by the bright appearance of the scattering filter structures as can be seen from comparing the zoomed regions in Figure 6(a, b), the expected position of TVFP noise is indicated by the blue arrow. Horizontal background artefacts are caused by the filter surface and the bright top of the mound as indicated by the orange arrows in Figure 6(b). A clean image is obtained via median based background estimation (Figure 6(c)). Since polarization was matched well already without spectral shaping a good image quality could be obtained. A small improvement is achieved when using Kaiser window apodization (magenta framed zoom in Figure 6(c)) and the filter surface as well as the mound top appear somewhat sharper due to reduced sidelobes. Positions of verti-

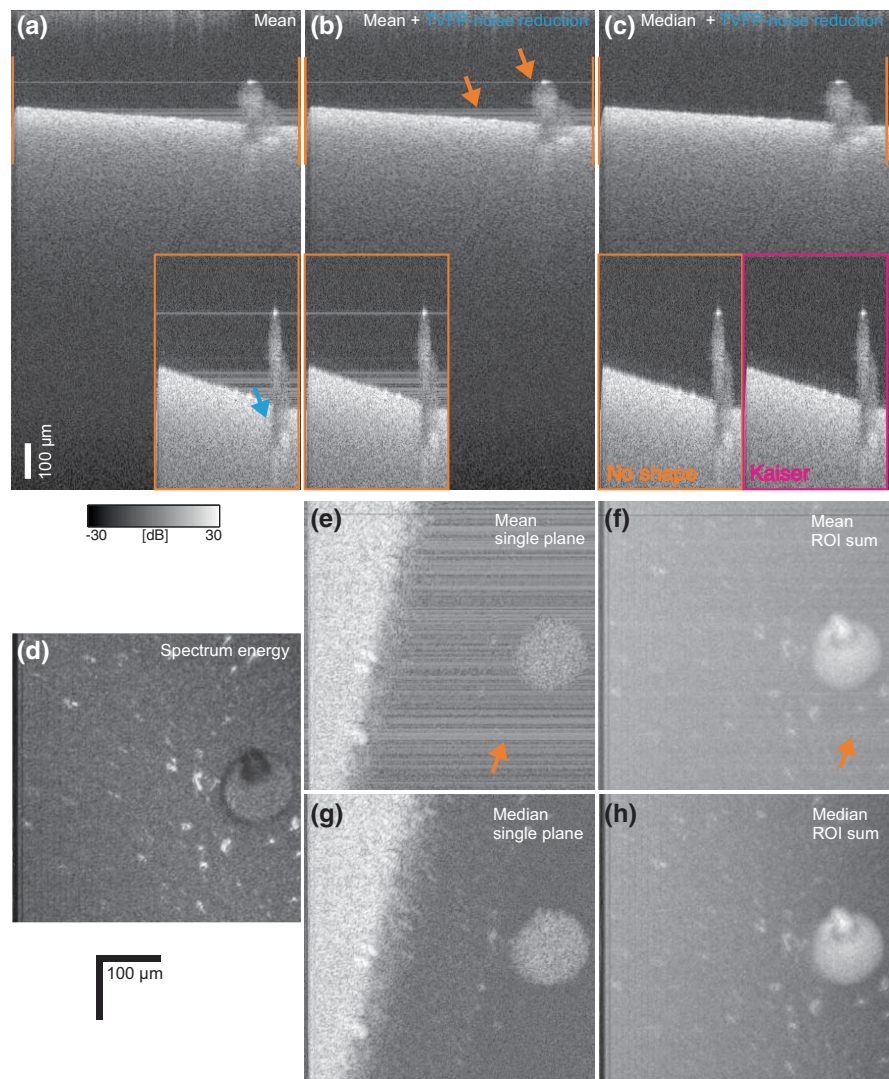


Figure 6 *Dictyostelium* on white nitrocellulose filter. Tomograms ($N_x = 512$, $N_z = 1024$ pixels) using (a) only mean based background correction, (b) additional TVFP reduction and (c) median background estimation and TVFP reduction; (c) right lower corner: magenta framed zoomed region after spectral shaping with a Kaiser window. *En face* views ($N_x = 512$, $N_y = 512$ pixels) using (d) spectrum energy, (e) single plane after mean background correction, (f) summation of ROI after mean, (g) single plane after median and (h) ROI sum after median.

cally zoomed regions are indicated by orange lines on left and right tomogram borders. They also indicate the ROI for *en face* view generation.

The *en face* image using spectrum energy (Figure 6(d)) provides an image that allows easy judgment of the field of view of the scanning microscope. The laser power was stable during imaging, thus no vertical intensity variations are visible in Figure 6(d). Background artefacts are visible on single and ROI summed *en face* images indicated by orange arrows in Figures 6(e) and (f) respectively. With median based estimation the background artefacts vanish (Figures 6(g) and (h)).

The camera induced TVFP noise floor causes a bright band on tomograms from RCG-5 cells grown on a microscope slide as can be seen in Figure 7(a). Thereby visualization of cells is disrupted (indicated by blue arrows) which causes problems for texture based cell analysis. With spread-domain filtering TVFP noise can be greatly reduced as depicted in

Figure 7(b). A horizontal background artefact on the upper surface is indicated by orange arrows in Figure 7(b), which disappears when using the median based technique (Figure 7(c)). Spectral shaping does not effect the image quality much as can be seen in the zoom-in of Figure 7(c). The noise floor is slightly reduced when using a Kaiser window, since noise from the spectral tails will be suppressed through the apodization.

Due to source power fluctuations the *en face* view from spectrum energy is disturbed by vertically varying intensity (Figure 7(d)). Median and mean *en face* views from a single plane or from averaging the ROI are almost identical since there are only a few background artefacts from the upper surface, therefore only the median based images are depicted in Figure 7(e), (f). Whereas in Figure 7(e) with a single parallel plane at a certain depth τ_k (just below the blue arrows in Figure 7(a)) only a small portion of the cells can be visualized, an aver-

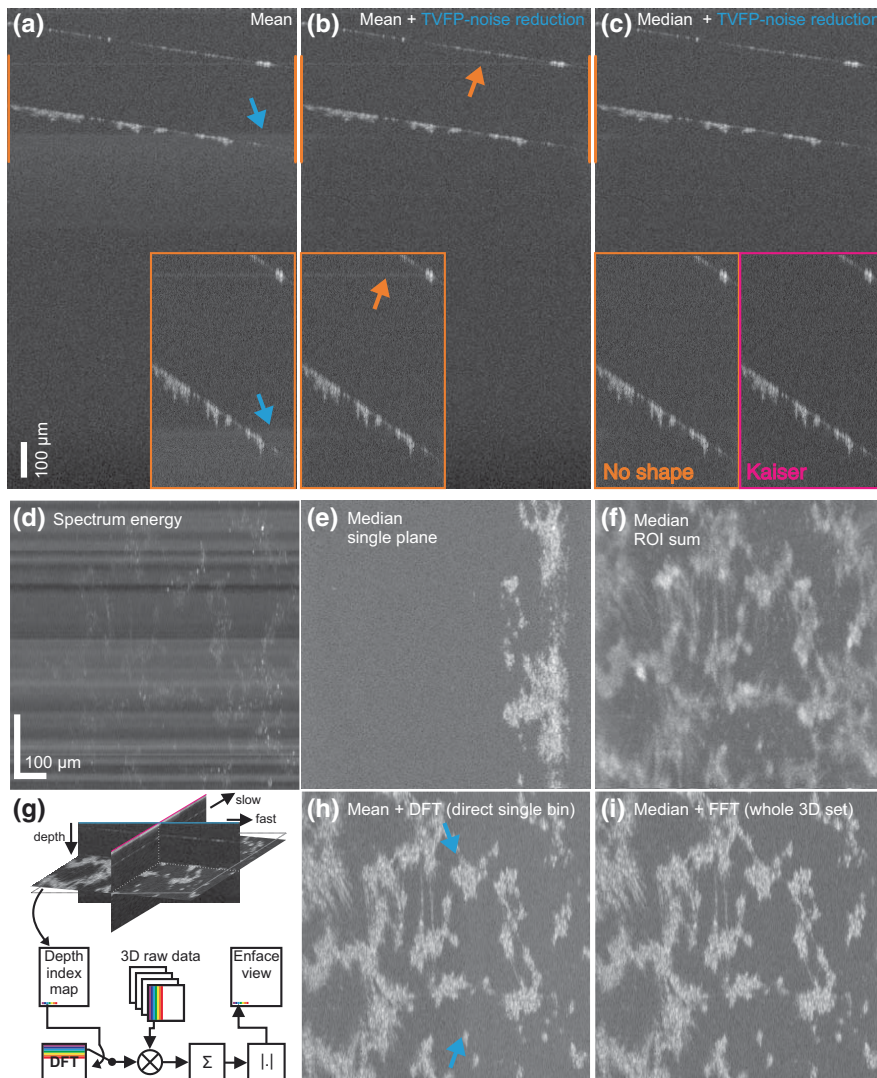


Figure 7 RGC-5 cells on glass coverslip. Tomograms ($N_x = 1024$, $N_z = 1024$ pixels) using (a) only mean-based background correction, (b) additional TVFP reduction and (c) median background estimation and TVFP reduction; (c) right lower corner: magenta framed zoomed region after spectral shaping with a Kaiser window. *En face* views ($N_x = 1024$, $N_y = 512$ pixels (vertically stretched)) using (d) spectrum energy, (e) single plane after median background correction, (f) summation of ROI after median, (h) single tilted plane after mean and single bin DFT and (i) single tilted plane after median and FFT of whole 3D data set. (g) Schematic of rapid *en face* view generation in arbitrary tilted plane from 3D raw data.

age image from the ROI obeys an increased blur in Figure 7(f). A tilted *en face* view directly below the microscope slide surface was extracted from the time domain 3D data set and does allow inspection of the cells with reduced blur (Figure 7(i)), processing time was about 12 minutes (Intel 2 GHz dual core processor, 8 GB RAM).

Figure 7(g) depicts the single bin discrete Fourier transform (DFT) based scheme [34]. It was adapted for direct calculation of the *tilted en face* view. For application of the scheme a fast and slow axis tomogram were extracted first. Segmentation of the microscope slide surface on these two perpendicular cross sections allowed calculation of a depth index map $\tau_{(x,y)}$ that defines the tilted surface. By adding a small offset the absolute depth was positioned to provide an *en face* image through the cells below the surface. The index map was then used to choose an individual DFT basis function for each position x and y , which was correlated with the specific raw

data line and the resulting magnitude value was filled at the corresponding *en face* view pixel.

The resulting *en face* view from the tilted plane is shown in Figure 7(h), using mean based background correction (no TVFP noise reduction). Besides an increased noise level (indicated by blue arrows), Figures 7(h) and (i) are comparable.

For $N_x \times N_y = 1024 \times 512$ pixels the processing time was reduced to about 47 seconds through direct application of the DFT. Further reduction can be expected by using specialized operations [34] or dedicated processing architectures. For real time view implementation, subsampling might be an option, i.e., when restricting the *en face* image to $N_x \times N_y = 256 \times 256$ pixels and correlating only 768 samples around the center frequency ($\omega_p \in \omega_{640} \dots \omega_{1408}$), which comprise most of the signal energy, processing times readily reduce to ~ 1 second without the need for dedicated hardware (implementation in Labview, Intel 2 GHz dual core processor, 8 GB RAM).

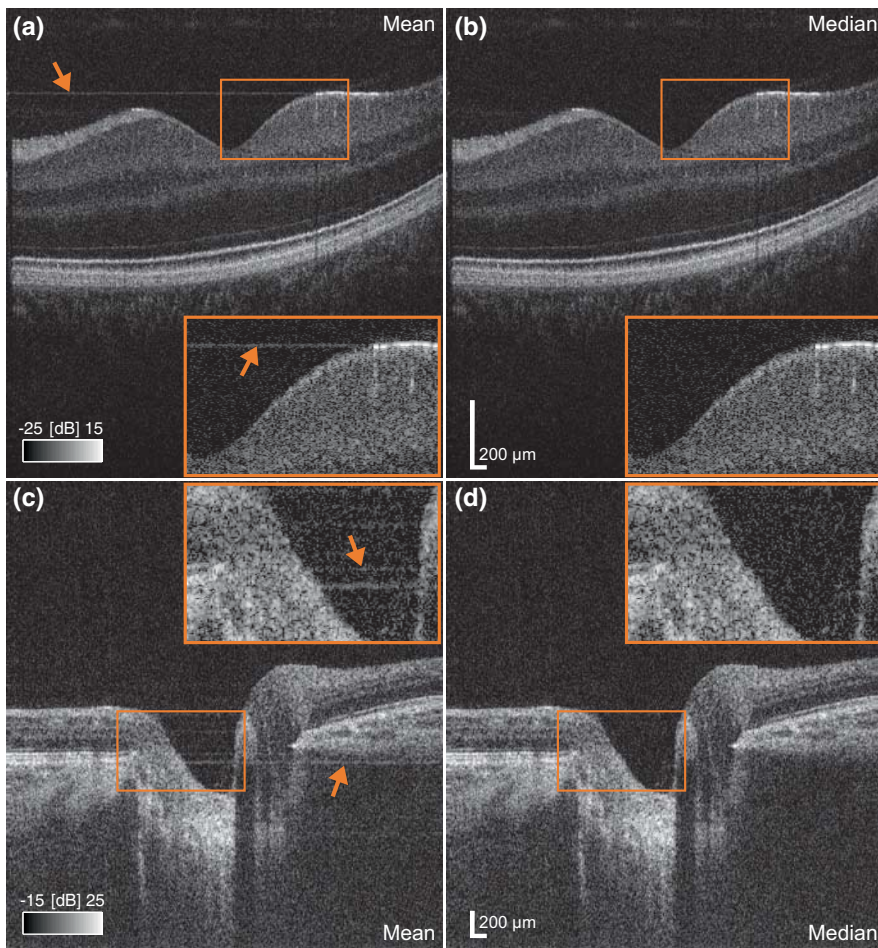


Figure 8 Retinal imaging *in vivo*. (a), (b) macula at 800 nm, (c), (d) optic disc at 1060 nm. (a), (c) Standard mean based background estimation with horizontal line artefacts indicated by orange arrows. (b), (d) Clean tomograms after applying the proposed median based background correction procedure. No additional image processing or noise reduction algorithms have been applied.

Also, retinal imaging benefits from the proposed background correction scheme as demonstrated in Figure 8. *In vivo* imaging was performed using two different systems at 800 nm and 1060 nm which have been described previously in [21, 35]. After standard processing with mean based background estimation horizontal line artefacts indicated by orange arrows arise from highly reflecting layers, i.e., inner limiting membrane in Figure 8(a) or retinal pigment epithelium in Figure 8(c). Clean tomograms are obtained after application of the proposed median based background estimation technique as depicted in Figure 8(c), (d).

5. Conclusion

Median based background elimination procedure greatly reduces transversal artefacts prominent in cell imaging using reflective substrates such as agar or nitrocellulose filters. High dynamic range of images also unveiled increased noise floor caused by camera specific TVFP noise that could be greatly re-

duced through application of a spread domain filter while minimally influencing morphology in final images. In cell-culture substrates with reflective interfaces, modulation artefacts from spectral shaping can be avoided by estimation of the effective spectral envelope from analytic signals. Specifically choosing a Kaiser window for envelope shaping results in high sidelobe suppression while retaining high axial resolution. Retinal imaging also benefits from the new background processing procedure.

Acknowledgments Contributions to cell cultivation and imaging by Debbie Tudor, Adrian Harwood and James Morgan are gratefully acknowledged. The authors thank Angelika Unterhuber, Marieh Esmaelpour Hajyar, Ling Wang, Aneesh Alex and Cristiano Torti for support and constructive discussions. This work was financially supported in part by Cardiff University; FP6-IST-NMP-2 STREPT (NANOUB – 017128), Action Medical Research (AP1110), DTI OMICRON (1544C), European Union project FUN OCT (FP7 HEALTH, contract no. 201880) and Grant N10606 of the Austrian Science Fund (NFN SISE).

Conflict of Interest W. Drexler and A. Tumlinson are working with Carl Zeiss Meditec.

Bernd Hofer received the Dipl.-Ing. and Dr.-techn. degree in electrical engineering from the University of Technology Vienna, Austria, in 2003 and 2010 respectively. From 2004 to 2005 he was with Two-Pi Signal Processing Applications GmbH in Vienna. 2006 he joined the Biomedical Imaging Group in the Department of Optometry and Vision Sciences, Cardiff University, Wales, UK. Since 2010 he is a member of the Center of Medical Physics and Biomedical Engineering, Medical University Vienna.

Boris Považay received his Masters degree 1998 from the University of Technology Vienna, Austria and continued his Ph.D. studies at the Medical University of Vienna on optical coherence tomography (OCT) for higher axial resolution and deeper penetration. 2006–2009 he held a lecturer position at the School of Optometry and Vision Sciences at Cardiff University and currently works at the Centre of Medical Physics and Biomedical Engineering at the Medical University Vienna. His research interests lie in the field of parallel frequency-domain techniques and optical encoding schemes for OCT, as well as the development and application of novel imaging methods with focus on ophthalmic and dermatological applications.

Boris Hermann obtained his M.Sc. in Physics in Berlin, Germany, in 2000 and his Ph.D. in electrical engineering at University of Technology, and Medical University, Vienna, Austria in 2006. Following postdoctoral research at Cardiff University, UK, in the field of OCT, he currently works at the Medical University, Vienna (Austria) with main focus on functional optical coherence tomography.

Sara M. Rey received a B.Sc. (Hons) in Neuroscience in 2006 and an M.Sc. in Biophotonics in 2007 from Cardiff University, UK. In 2007 she entered the four-year Ph.D. programme in interdisciplinary technology in regenerative medicine at Cardiff University. She is currently working on noninvasive imaging of cells in the Department of Biosciences and the Biomedical Imaging Group from the School of Optometry and Vision Sciences at Cardiff University.

Vedran Kajić received his B.Sc. in the faculty of Electrical Engineering and Computing, University of Zagreb, Croatia, in 2007. He currently prepares for his Ph.D. in the field of computer science with main focus on segmentation of optical coherence tomography images.

Alexandre Tumlinson received his Ph.D. from the University of Arizona, Tucson (US). Following three years working as Research Associate in Cardiff University (UK), he currently is employed at Carl Zeiss Meditec.

Kate Powell received her PhD in Neuroscience from the University of Newcastle, Australia and currently

works as a Research Associate investigating mitochondrial optic neuropathies in the Visual Neuroscience and Molecular Biology group, School of Optometry, Cardiff University, UK.

Gerald Matz received the Dipl.-Ing. and Dr. techn. degrees in electrical engineering in 1994 and 2000, respectively, and the Habilitation degree for communication systems in 2004, all from Vienna University of Technology, Vienna, Austria. Since 1995, he has been with the Institute of Communications and Radio-Frequency Engineering, Vienna University of Technology, where he currently holds a tenured position as Associate Professor. He has published more than 130 papers in international journals, conference proceedings, and edited books. His research interests include wireless communications and sensor networks, statistical signal processing, and information theory.

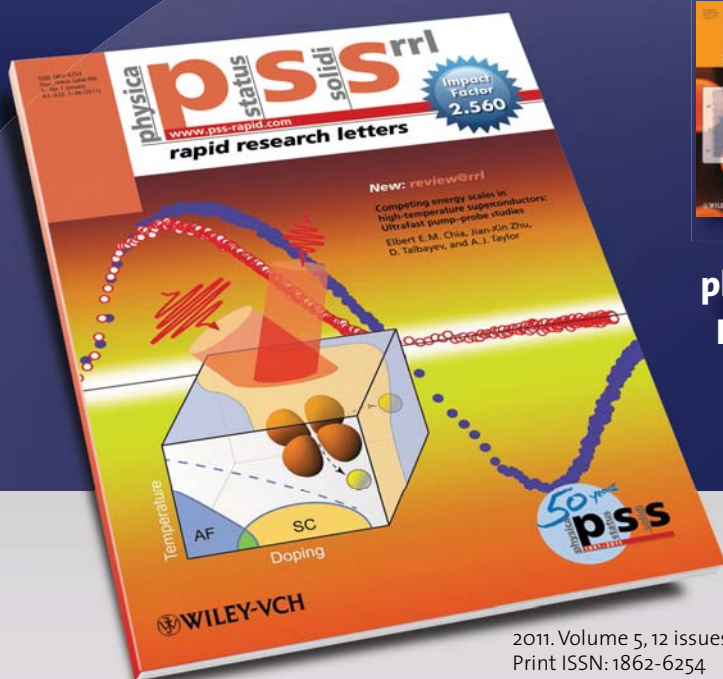
Wolfgang Drexler is currently Head of the Center for Medical Physics and Biomedical Engineering and Professor of Medical Physics, Medical University Vienna, Austria. So far his research group has accomplished pioneering work in the development of OCT. He spent two years at MIT, Cambridge, USA, and was for four years the Director of the Christian Doppler Laboratory, followed by four years Full Professor of Biomedical Imaging at Cardiff University, Wales, UK. He received the Austrian START Award in 2001 and the COGAN Award in 2007. He is a member of the Austrian Academy of Science and has published more than 120 papers in peer-reviewed journals.

References

- [1] W. Tan, A. L. Oldenburg, J. J. Norman, T. A. Desai, and S. A. Boppart, *Opt. Express* **14**, 7159–7171 (2006).
- [2] C. Vinegoni, T. Ralston, W. Tan, W. Luo, D. L. Marks, and S. A. Boppart, *Appl. Phys. Lett.* **88**, 053901 (2006).
- [3] C. Y. Xu, C. Vinegoni, T. S. Ralston, W. Luo, W. Tan, and S. A. Boppart, *Opt. Lett.* **31**, 1079–1081 (2006).
- [4] W. Tan, C. Vinegoni, J. J. Norman, T. A. Desai, and S. A. Boppart, *Microsc. Res. Techniq.* **70**, 361–371 (2007).
- [5] S. M. Rey, B. Považay, B. Hofer, A. Unterhuber, B. Hermann, A. Harwood, and W. Drexler, *J. Biophoton.* **2**, 370–379 (2009).
- [6] B. Považay, K. Bizheva, A. Unterhuber, B. Hermann, H. Sattmann, A. F. Fercher, W. Drexler, A. Apolonski, W. J. Wadsworth, J. C. Knight, P. S. J. Russell, M. Vetterlein, and E. Scherzer, *Opt. Lett.* **27**, 1800–1802 (2002).
- [7] A. Dubois, G. Moneron, K. Grieve, and A. C. Boccara, *Phys. Med. Biol.* **49**, 1227–1234 (2004).

- [8] A. D. Aguirre, P. Hsiung, T. H. Ko, I. Hartl, and J. G. Fujimoto, *Opt. Lett.* **28**, 2064–2066 (2003).
- [9] M. Wojtkowski, V. J. Srinivasan, T. H. Ko, J. G. Fujimoto, A. Kowalczyk, and J. S. Duker, *Opt. Express* **12**, 2404–2422 (2004).
- [10] T. S. Ralston, D. L. Marks, P. S. Carney, and S. A. Boppart, *Nat. Phys.* **3**, 129–134 (2007).
- [11] P. D. Woolliams, R. A. Ferguson, C. Hart, A. Greenwood, and P. H. Tomlins, *Appl. Optics* **49**, 2014–2021 (2010).
- [12] M. A. Choma, A. K. Ellerbee, C. Yang, T. L. Creazzo, and J. A. Izatt, *Opt. Lett.* **30**, 1162–1164 (2005).
- [13] E. J. McDowell, A. K. Ellerbee, M. A. Choma, B. E. Applegate, and J. A. Izatt, *J. Biomed. Opt.* **12**, 044008 (2007).
- [14] A. K. Ellerbee, T. L. Creazzo, and J. A. Izatt, *Opt. Express* **15**, 8115–8124 (2007).
- [15] C. Joo, K. H. Kim, and J. F. Boerde, *Opt. Lett.* **32**, 623–625 (2007).
- [16] B. Potsaid, I. Gorczynska, V. J. Srinivasan, Y. Chen, J. Jiang, A. Cable, and J. G. Fujimoto, *Opt. Express* **16**, 15149–15169 (2008).
- [17] B. Považay, B. Hofer, C. Torti, B. Hermann, A. R. Tumlinson, M. Esmaelpour, C. A. Egan, A. C. Bird, and W. Drexler, *Opt. Express* **17**, 4134–4150 (2009).
- [18] I. Grulkowski, I. Gorczynska, M. Szkulmowski, D. Szlag, A. Szkulmowska, R. A. Leitgeb, A. Kowalczyk, and M. Wojtkowski, *Opt. Express* **17**, 23736–23754 (2009).
- [19] R. K. Wang and Z. Ma, *Phys. Med. Biol.* **51**, 3231–3239 (2006).
- [20] B. Hofer, PhD thesis, Technical University Vienna (Austria), 2010.
- [21] B. Hofer, B. Považay, B. Hermann, A. Unterhuber, G. Matz, and W. Drexler, *Opt. Express* **17**, 7–24 (2009).
- [22] N. A. Nassif, B. Cense, B. H. Park, M. C. Pierce, S. H. Yun, B. E. Bouma, G. J. Tearney, T. C. Chen, and J. F. Boerde, *Opt. Express* **12**, 367–376 (2004).
- [23] P. Bello, *IEEE Trans. Commun. Syst.* **11**, 360–393 (1963).
- [24] A. C. Akcay, J. P. Rolland, and J. M. Eichenholz, *Opt. Lett.* **28**, 1921–1923 (2003).
- [25] A. C. Akcay, E. Clarkson, and J. P. Rolland, *Appl. Optics* **44**, 7573–7580 (2005).
- [26] M. Bashkansky, M. Duncan, J. Reintjes, and P. Battle, *Appl. Optics* **37**, 8137–8138 (1998).
- [27] J. F. Boerde, C. E. Saxer, and J. S. Nelson, *Appl. Optics* **40**, 5787–5790 (2001).
- [28] R. Tripathi, N. Nassif, J. S. Nelson, B. H. Park, and J. F. Boerde, *Opt. Lett.* **27**, 406–408 (2002).
- [29] D. L. Marks, P. S. Carney, and S. A. Boppart, *J. Biomed. Opt.* **9**, 1281–1287 (2004).
- [30] D. L. Marks, A. L. Oldenburg, J. J. Reynolds, and S. A. Boppart, *Appl. Optics* **42**, 204–217 (2003).
- [31] M. Szkulmowski, M. Wojtkowski, T. Bajraszewski, I. Gorczynska, P. Targowski, W. Wasilewski, A. Kowalczyk, and C. Radzewicz, *Opt. Comm.* **246**, 569–578 (2005).
- [32] Y. Yasuno, Y. Hong, S. Makita, M. Yamanari, M. Akiba, M. Miura, and T. Yatagai, *Opt. Express* **15**, 6121–6139 (2007).
- [33] R. R. Krishnamoorthy, P. Agarwal, G. Prasanna, K. Vopat, W. Lambert, H. J. Sheedlo, I. H. Pang, D. Shade, R. J. Wordinger, T. Yorio, A. F. Clark, and N. Agarwal, *Mol. Brain Res.* **86**, 1–12 (2001).
- [34] R. G. Chelliyil, T. S. Ralston, D. L. Marks, and S. A. Boppart, *J. Biomed. Opt.* **13**, 044013 (2008).
- [35] B. Považay, B. Hermann, B. Hofer, V. Kajić, E. Simpson, T. Bridgford, and W. Drexler, *Invest. Ophthalmol. Vis. Sci.* **50**, 1856–1863 (2009).

The latest member of the physica status solidi journals



2011, Volume 5, 12 issues.
Print ISSN: 1862-6254
Online ISSN: 1862-6270



**physica status solidi RRL –
Rapid Research Letters, the fastest
peer-reviewed publication
medium in solid state physics**

EDITOR-IN-CHIEF

Martin Stutzmann,
München, GER

EDITORIAL BOARD

Martin S. Brandt, München, GER
Marília J. Caldas, São Paulo, BR
Elvira Fortunato, Caparica, PT
Chennupati Jagadish, Canberra, Australia
Chun-Sing Lee, Hong Kong, China
Shuit-Tong Lee, Hong Kong, China
Pablo Ordejón, Barcelona, ES
John Robertson, Cambridge, UK
Michael S. Shur, Troy, USA
James S. Speck, Santa Barbara, USA
Christian Thomsen, Berlin, GER
John I. B. Wilson, Edinburgh, UK

► offers extremely fast publication
times: typically 14 days from sub-
mission to first editorial decision,
5 days to final online publication.

This is definitely a world record for Letter
journals in solid state physics!
Peer-review by two independent referees
guarantees strict quality standards.

► communicates important findings
with a high degree of novelty and need
for express publication, as well as other
results of immediate interest to the
solid state physics and materials science
community.

► **Submit your manuscript now!**

www.pss-rapid.com

 **WILEY**  **ONLINE LIBRARY**
wileyonlinelibrary.com

 **WILEY-BLACKWELL**

For subscription details please contact **Wiley Customer Service:**

- cs-journals@wiley.com (Americas, Europe, Middle East, Africa, Asia Pacific)
- service@wiley-vch.de (Germany, Austria, Switzerland)
- cs-japan@wiley.com (Japan)

With an Impact Factor of
2.560* *pss RRL* is the
most highly cited journal
publishing exclusively
Letter articles in condensed
matter physics."

*2009 Journal Citation Reports®
(Thomson Reuters, 2010)